Spin fluctuations, geometrical size effects, and zero-field topological order in textured MnSi thin films

J. López-López,[1] Juan M. Gomez-Perez,[1] A. Álvarez,[1] Hari Babu Vasili,[2] A. C. Komarek,[3] L. E. Hueso,[1,4] Fèlix Casanova,[1,4] and S. Blanco-Canosa[1,4,5,*]

[1]*CIC nanoGUNE, 20018 Donostia-San Sebastian, Basque Country, Spain*
[2]*ALBA Synchrotron Light Source, Cerdanyola del Vallès, 08290 Barcelona, Catalonia, Spain*
[3]*Max Planck Institute for Chemical Physics of Solids, Nöthnitzerstrasse 40, 01187 Dresden, Germany*
[4]*IKERBASQUE, Basque Foundation for Science, 48013 Bilbao, Basque Country, Spain*
[5]*Donostia International Physics Center, DIPC, 20018 Donostia-San Sebastian, Basque Country, Spain*

(Received 18 August 2018; revised manuscript received 22 March 2019; published 29 April 2019)

Noncollinear magnetic structures with broken inversion symmetry have recently revolutionized the field of spintronics. Among them, transition metal monosilices and germanides are potential candidates due to their nontrivial spin textures. Here we report the growth and magnetic and electronic characterization of high-quality (111)-oriented thin films of MnSi by magnetron sputtering. While thicker films order magnetically similar to their bulk counterpart and according to previous reports in literature, x-ray magnetic circular dichroism measurements indicate that 30-nm-thick films do not develop long-range magnetic order, presumably due to magnetic frustration introduced by domains of different chiralities and spin disorder. X-ray absorption spectroscopy shows a stabilization of Mn^{+} oxidation state in epitaxial thin films evidencing different electronic structure as compared with bulk MnSi. Field- and angular-dependent magnetoresistance support a magnetically disordered scenario, while Hall resistivity develops features of zero-field topological order formerly ascribed to skyrmions. Our results highlight the importance of geometrical size effects and spin disorder in noncentrosymmetric magnets and suggest that the topological Hall effect in thin films cannot be taken as the sole criterium for the assignment of nontrivial magnetic structures.

DOI: 10.1103/PhysRevB.99.144427

I. INTRODUCTION

The discovery of a skyrmion lattice [1] and its manipulation with low current densities [2] promoted noncollinear magnetic structures as promising candidates for information processing and data storage [3]. Special attention is devoted to the *B*20 crystals [4,5], multiferroics [6], alloys [7,8], and artificial structures lacking inversion symmetry. From the microscopic point of view, broken inversion symmetry introduces a Dzyaloshinkii-Moriya interaction (DMI) $\frac{D}{S}\mathbf{M}\cdot(\nabla\times\mathbf{M})$, where D is the Dzyaloshinkii constant and $\mathbf{M}$ the magnetization, which allows for orthogonal spin interactions. Besides, the isotropic Heisenberg exchange interaction favors parallel spin alignments, thus, the competition among these quantum mechanical interactions, thermal and magnetic energies leads to complex magnetic structures with nontrivial topological magnetotransport properties [9].

In noncentrosymetric cubic monosilices and monogermanides [A(Si,Ge), A= Mn, Fe, Co], the magnetic phase diagram encompasses magnetic phases ranging from helicoidal, conical to fully polarized states depending on the strength of the magnetic field [4,5,10]. For the particular case of MnSi at zero magnetic field, the competition between the DMI and the Heisenberg exchange interaction produces a helical magnetic order below the Curie temperature, $T_C = 30$ K, with a wavelength of the helix $\lambda_D \sim 18$ nm [11] determined by the ratio of the energy terms $2\pi/Q \propto A/D$, where A is the *exchange stiffness* and Q is the propagation vector. Q points along [111] direction with the magnetic moments lying perpendicular to it. If an external magnetic field is applied perpendicular to [111], Q rotates in the direction of the magnetic field and becomes parallel to field at $H_s^{\parallel} = 0.1$ T. Above the critical field applied along the [111] direction, $H_c^{\perp}$, the magnetic moments form a conical phase, which collapses into a ferromagnetic state at $H_s^{\perp} = 0.6$ T. In a small region of the H-T phase diagram, strong evidences for the presence of solitonic states, termed *skyrmions*, have been revealed by means of neutron scattering [1], ac susceptibility [12], and Hall effect [13]. Lorentz microscopy imaged the helimagnetic and skyrmion phase under a moderate normal magnetic field in thin films [14] and nanometer-polished MnSi [15]. This suggests that size effects, strain and magnetic anisotropies play a crucial role in stabilizing these spin textures.

In order to increase the skyrmion region, theory predicts that uniaxial strain introduced by the epitaxial growth suppresses the helical order and thermodynamically stabilizes skyrmion lattices. Micromagnetic simulations show that helicoids and skyrmion states are the most stable solutions for large values of the anisotropy ratio (K/K_0) [16], K stands for the uniaxial anisotropy and K_0 is the anisotropy value defined as $K_0 = H_d/2M$, where H_d is a characteristic field depending on the D and A ratio and M is the magnetization. Therefore, tuning the magnetic anisotropy of noncentrosymmetric

*sblanco@dipc.org

magnets through strain engineering opens the possibility to stabilize nontrivial chiral modulations and complex spin textures [17]. More recent numerical simulations show that multidimensional solitons and particlelike states can be stabilized at interfaces and surfaces of chiral magnets due to finite size effects and reduction of dimensionality [18]. Thereby, much of the research on the *B*20 alloys has been dedicated to the stabilization and detection of these new topological magnetic states in thin films [19–21], as those are required for skyrmion manipulation in spintronic devices.

Besides, the skyrmion lattice is correlated with the emergence of a new topological electrodynamics [9]. The conduction electrons acquire a real-space Berry phase as they adiabatically follow the local magnetization of the knotlike spin textures. This introduces an effective field, B_{eff} that gives rise to the topological Hall effect, THE. This Hall effect adds to the ordinary Hall effect (OHE) from the deflection of the electrons under magnetic field and the anomalous Hall effect (AHE) from the intrinsic magnetism of the ferromagnetic material [22]. Therefore it has been generally accepted that the detection of THE is an indication of the presence of nontrivial spin textures and, in particular, skyrmions. Nevertheless, some authors argue that the scattering from the conical phase is responsible for the observed anomalies in the Hall resistivity [23] and the microscopy results can be explained by structural artifacts. In addition, polarized neutron reflectometry [24,25] have determined that the ground state of MnSi thin films is helical and propagates along the out-of-plane [111] direction, ruling out the skyrmion phase since no first-order magnetic phase transitions are observed.

However, despite the huge amount of research on the dependence of the topological properties of MnSi with the variation of the magnetic anisotropy and strain, the electronic structure of MnSi when grown as thin films and its relationship with the topological order has been largely overlooked. Since MnSi has a mixed valence ground state [26] with comparable energy scales, strain engineering, interface nucleation or defects can tune the balance among the orbital occupations and influence the magnetic properties and the emergence of new topological order. Moreover, the effects driven by the electronic inhomogeneity are neglected in the calculation of the induced anisotropies which modify the ground state of thin MnSi films. In order to gain more information about the electronic structure, scattering mechanisms and its relationship with the anomalous Hall resistivity, we have grown and characterized high-quality MnSi thin films. We find that, according to x-ray absorption spectroscopy (XAS), the Mn^{+} oxidation state (d^6) is stabilized in MnSi epilayers as compared with bulk MnSi. X-ray magnetic circular dichroism (XMCD) shows no sign of magnetic saturation up to 6 T for thicknesses below double of the wavelength of the helical order. In addition, a combination of field- and angular-dependent magnetoresistance indicate scattering from spin fluctuations and spin disorder rather than scattering from conical or helical phases. Remarkably, the Hall resistivity shows indications of extended zero-field topological Hall effect, as previously reported for FeGe [27] and MnGe [28]. Our combination of transport and spectroscopic results allows us to draw a picture correlating the electronic structure, geometrical size effects, spin fluctuations and disorder crucial for the interpretation of the Hall signal in noncentrosymetric MnSi thin films.

In the next section, we describe the growth of MnSi thin films as well as the experimental methods. The presentation of the results is given in Sec. III (structural characterization, magnetization, susceptibility, electronic structure and XMCD, magnetoresitance and Hall effect) followed by discussion and conclusions in Secs. IV and V.

II. EXPERIMENTAL METHODS

Textured (111) MnSi films with thickness, t, that range between 15 and 300 nm were grown by off-axis magnetron sputtering on high-resistive (> 10 kΩ cm) Si (111) substrates with a base pressure of 2×10^{-9} mbar. Unlike molecular beam epitaxy (MBE) and previous works which evaporated a seed layer of the metal continued with co-evaporation of Mn and Si, we used a pure stoichiometric MnSi target, previously tested to confirm the bulk properties of MnSi. Si wafers were etched in HF to remove the native SiO_2 layer. The deposition was performed at 440 °C followed by an annealing at the same temperature for 1 hour. After cooling to room temperature, MnSi films were capped with an amorphous SiO_2 protective layer to prevent oxidation. Contact pads and Hall bars (width 10 μm, length 0.3 mm) were patterned by means of photolitography and Ar-ion milling. *In situ* Ti-Au pads were deposited in high vacuum of the ion-miller chamber. MnSi single crystals have been grown at the MPI-CPfS using a high-pressure mirror furnace (Scidre). Magnetization and magnetotransport measurements were carried out in a liquid-He cryostat at temperatures between 2 and 300 K and magnetic fields up to 9 T. X-ray absorption (XAS) and x-ray magnetic circular dichroism (XMCD) measurements in MnSi films and *in-vacuum* cleaved bulk crystals were performed at the Mn $L_{2,3}$ edge at the BOREAS BL29 beamline at ALBA synchrotron.

III. RESULTS

A. Structural characterization

The structure of the MnSi films was characterized by x-ray reflectivity (XRR), x-ray diffraction (XRD), and high-resolution transmission electron microscopy (HRTEM). As depicted in Fig. 1(a), the expected epitaxial orientation is observed following the (111) reflection of MnSi in the diffraction pattern, ruling out any impurity phase and confirmed by electron diffraction (not shown). The interplanar lattice spacing of $d_{111} = 2.625$ Å, gives an out-of-plane lattice parameter of 4.546(2) Å, which closely matches that of the bulk, 4.558 Å, indicating less than 0.3% compressive strain. In addition, the out-of-plane lattice parameter is thickness independent [Fig. 1(a), inset] ruling out strain effects which have been predicted to tune the anisotropy and exchange interactions [17]. A rocking curve for the MnSi (111) peak (not shown) presents a mosaicity of 0.2°, showing a high degree of texture. The structure of the MnSi layer was also characterized by HRTEM. Figure 1(b) shows an image of a 30-nm-thick film, where the interface between the MnSi layer and Si substrate reveals an epitaxial growth along the (111) direction. The crystalline quality of the MnSi epilayer is excellent and no misfit edge dislocations or stacking faults at the

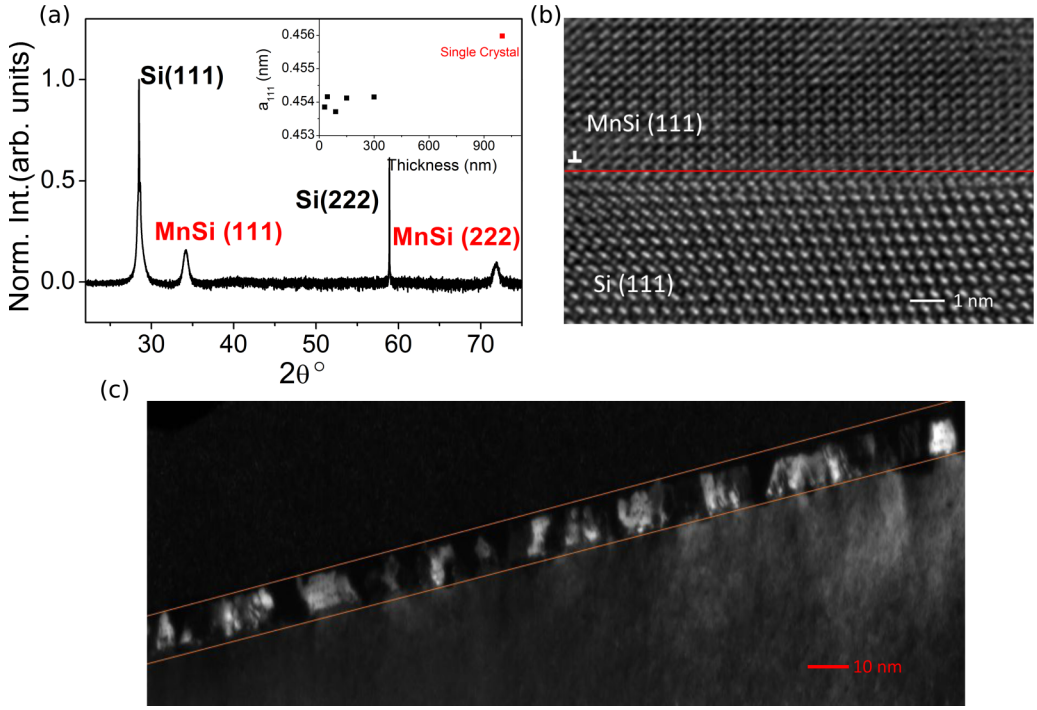

FIG. 1. (a) 2θ-ω XRD scan of 30-nm-thick MnSi thin film grown on Si(111). (b) HRTEM image viewed near the MnSi(111)/Si(111) interface observing the (111) crystallographic planes. (c) Dark field image of the MnSi thin film, observing the contrast between domains of opposite chiralities (bright and dark regions).

MnSi/Si interface were observed. Dark-field TEM images, Fig. 1(c), show that both left- and right-handed domains with ∼10–30 nm, typical of noncentrosymmetric crystal structures, are present.

B. Magnetometry

We now proceed with the study of the magnetic properties of MnSi films. Magnetization, M, was measured in a conventional VSM-SQUID. Same as previous studies, the magnetization with the magnetic field perpendicular, $H \| \text{Si}(111)$, and parallel to the film surface, $H \perp \text{Si}(111)$, turns out to be challenging to track due to the low magnetic moment of Mn and the large diamagnetic contribution of the substrate. Several authors have determined separately the substrate contribution in the high-field region of the $M(H)$ loops, far above the saturation field and subtracted to the experimental data [see bottom inset of Fig. 2(b)]. This procedure gives a reliable estimation of the saturated magnetic moment for thick films but fails for thinner epilayers. In this section, we will focus on the magnetization obtained by VSM for 150-nm-thick MnSi film. Thinner epilayers will be treated in the next section. In Fig. 2(a), we plot the temperature dependence of M for a 150-nm-thick film with an out-of plane magnetic field of 0.01 T. The transition temperature T_C is 34 K, similar to the bulk value (∼30 K) and lower than the value reported for MBE samples [19]. The value of T_C is independent of the film thickness, suggesting negligible finite size effects and strain. In- and out-of-plane magnetization versus field [$M(H)$], perpendicular and parallel to (111) direction, respectively, is plotted in Fig. 2 b evidencing a (111) hard axis. At low temperature ($T = 5$ K), the 150-nm-thick film has a saturated magnetic moment of 0.4 μ_B, similar to the value reported in literature for MnSi thin films [29] and in good agreement with bulk [12]. Having a closer look to the $M(H)$ curves, a remanent magnetization for in-plane measurements of $M_r = 0.1\ \mu_B$/Mn and a hysteresis of 0.05 T is also observed [top inset of Fig. 2(b)]. The presence of an in-plane M_r is consistent with a helical magnet whose magnetic moments are in plane and spiral out-of-plane.

The pitch of the helical order can be calculated from the values of M_r since Q points normal to the film surface; i.e., parallel to [111]. Following the analysis developed by E. Karhu *et al.* [29] and Huang *et al.* [30], for a helical magnetic order propagating parallel to $Q \| [111]$, we obtain a helical wavelength $2\lambda_D = 2\pi/Q \sim 18$ nm, providing that the out-of-plane saturation field $H_s^{\perp} = AQ^2$, and A is the spin wave exchange stiffness [31,32]. This value nicely matches the bulk wavelength and confirms that our sputtered thick MnSi films develop *bulk* properties. Nevertheless, while M_s is comparable to the bulk value, the in- and out-of-plane saturation fields, 0.7 and 2.4 T, respectively, are larger than the bulk, 0.6 T. With this information, we calculate the uniaxial anisotropy in MnSi, as theories suggest that it can stabilize skyrmion phases. The uniaxial anisotropy, K, determined from M_s and the in-plane and out-of-plane saturation fields ($H_s^{\|}$ and $H_s^{\perp}$, respectively) and the *effective stiffness* of the conical phase, K_0, are given by [29]

$$K = -\frac{Ms}{3}\left(H_s^{\perp} - H_s^{\|} - 4\pi Ms - \frac{K_m}{M_s}\right), \quad (1)$$

$$K_0 = \frac{Ms}{6}\left(H_s^{\perp} + 2H_s^{\|} - 4\pi Ms + \frac{2K_m}{M_s}\right), \quad (2)$$

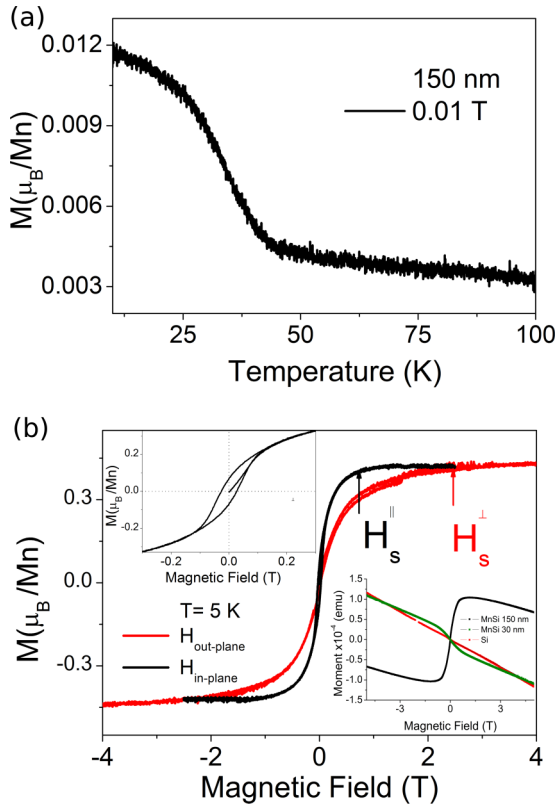

FIG. 2. (a) Out-of-plane magnetization as a function of temperature for 150-nm-thick MnSi film at $H = 0.01$ T ($T_C = 34$ K). (b) In- and out-of-plane magnetization hysteresis curves at 5 K showing the in- ($H_s^{\parallel}$) and out-of-plane ($H_s^{\perp}$) saturation fields, respectively. (Top inset) Zoom-in of the $H_s^{\parallel}$ at low fields, highlighting M_r. (Bottom inset) Bare $M(H)$ curve for 150-nm (black) and 30-nm-MnSi (green) films before subtraction of the Si substrate (red).

where K_m is the *stray field* contribution that depends on A and D and is defined

$$K_m = Ms^2 \frac{\lambda_D}{t}\left[1 - \exp\left(-\frac{2\pi t}{\lambda_D}\right)\right]. \quad (3)$$

K is found to be positive showing that it is of easy plane type but it cannot have its origin only in magnetoelastic effects since the strain induced by the substrate is negligible, as observed by XRD. Micromagnetic simulations show that a positive K increases the DMI, suppresses the conical phase and stabilizes skyrmions at lower magnetic fields [16]. For 150-nm-thick MnSi film, we obtain $K/K_0 \sim 1.19(3)$, similar to the value reported in 30-nm-thick FeGe films with zero-field topological Hall effect [30] and the, within theoretically suggested, region of the phase diagram with first order transitions between helicoidal and skyrmion phases. However, no peaks in the field dependence of the static susceptibility dM/dH are observed, ruling out first-order magnetic phase transitions below the saturation field $H_s^{\perp}$. Therefore, additional different electronic structure or surface/interface effects can shape to the quantitative modulation of the phase diagram.

As observed in the bottom inset of Fig. 2(b), the high-field susceptibility in MnSi films is never saturated due to the Si substrate contribution. Therefore, separating the magnetization of the film from the one of the substrate for thicknesses similar to those which report zero-field topological order gives rise to a high level of uncertainty in the determination of the saturated magnetic moment of Mn. This is evidenced for 30-nm MnSi film, which shows a large diamagnetic contribution coming from the Si substrate [bottom inset of Fig. 2(b)].

C. Electronic structure and XMCD

In order to unambiguously measure the magnetic properties of thinner MnSi films, we have performed a comprehensive electronic and magnetic characterization by means of XAS and XMCD. Energy dependent absorption spectra is an element-specific technique that allows to determine the electronic ground state of complex materials by making use of the dipole selection rules. In the soft x-ray region, this makes XAS an extremely sensitive local probe to study the electronic structure and valence, spin, and orbital state in transition metal and $4f$ rare-earth compounds [33]. The absorption data have been taken by measuring the drain current (total electron yield, TEY) and the photons exerted from the sample (fluorescence yield, FY) with the incident beam perpendicular to the sample surface, hence parallel to (111) crystallographic axis and the external magnetic field [Fig. 3(a)]. TEY measures the total number of electrons emitted from the sample due to fluorescent decay of Mn $3d \rightarrow 2p$ and $2p \rightarrow 3s$ levels, and is mostly surface sensitive within a depth of 2–3 nm, unlike FY which detects the number of emitted fluorescence photons and is proportional to the number of absorbed photons within the penetration depth of the soft x-ray photons (~50 nm). Thereby, FY can be considered a bulk measurement but suffers from self-absorption processes. Independently of the detection mode, the isotropic XAS spectra, i.e., $(C^+ + C^-)/2$, consists of two main peaks corresponding to the $2p_{3/2}$ (642 eV) and $2p_{1/2}$ (653 eV) spin-orbit split components of the $2p$ core level, see Fig. 3(b) for a comparison of bulk, 150-nm and 30-nm MnSi. Bulk MnSi shows a broad XAS spectrum due to transitions into the continuum of states and a peak of intensity at 639.5 eV. On the other hand, the L_3 edge of 150-nm- and 30-nm-thick films develop also a sizable intensity at 641 and a shoulder at 643.5 eV [Fig. 3(i)], presumably due to localization of electronic states. This assumption is based on the narrowing of the XAS spectrum in the film as compared with the bulk and further supported by the enhancement of the electrical resistivity for thinner films, as we will see later. Nevertheless, a different shape of the L_2 edge at both TEY (surface sensitive) and FY (bulk sensitive) is also evident, indicating that an electronic reconstruction in thin films can happen.

Former XAS spectroscopy and photoemission provided experimental evidence that bulk MnSi has a mixed valence ground state not captured by the standard LDA approach [26]. In order to gain deeper information of the electronic ground state of our thin MnSi films, we have performed cluster calculations in the cubic crystal field for the atomic like $2p^6 - 3d^{\delta} \rightarrow 2p^5 3d^{\delta+1}$ transitions using the crystal-field theory implemented in QUANTY [34,35]. The method accounts for the intraatomic $3d - 3d$ and $2p - 3d$ Coulomb energies (Slater integrals), magnetic exchange interactions,

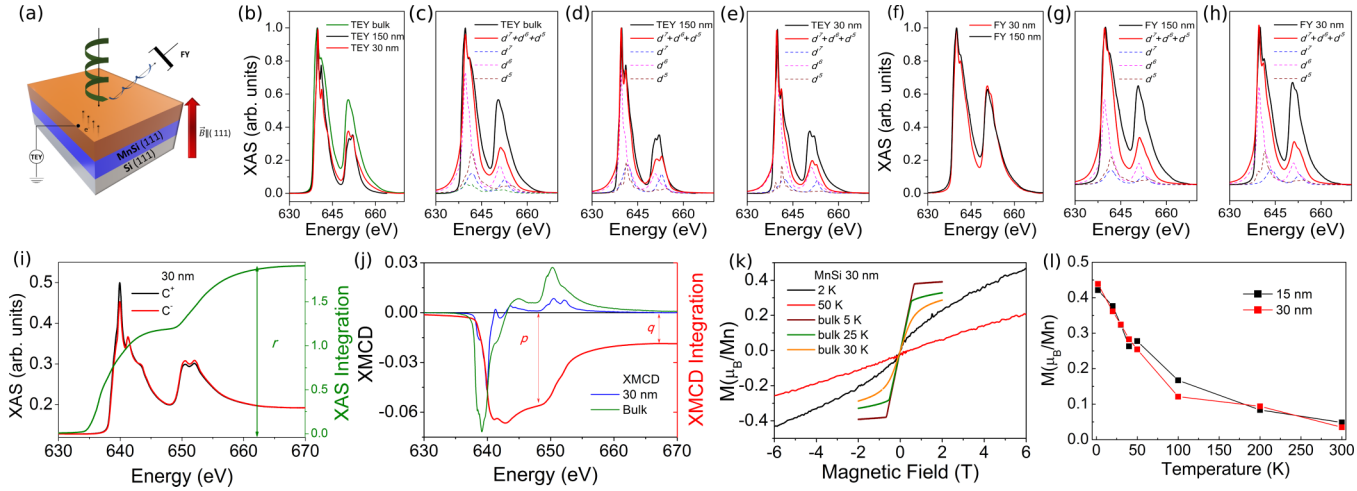

FIG. 3. (a) Sketch of the geometry of the x-ray magnetic circular dichroism (XMCD) measurements. The magnetic field is applied parallel to the beam of circularly polarized photons and (111) crystallographic axis of MnSi. (b) X-ray absorption spectrum (XAS) at the Mn L edge for bulk MnSi (green), 150 nm (black) and 30 nm (red) curves in TEY detection mode. The transitions occur from the spin-orbit split $2p$ core shell to empty conduction band states. [(c)–(e)] Simulated XAS spectrum obtained from the sum of d^7, d^6, and d^5 contributions (red spectrum) following Ref. [26] for bulk and MnSi films. Broken lines correspond to the spectral weight contribution of each valence state. (f) Comparison of the FY-XAS spectra for 150 and 30-nm MnSi films. (g,h) Simulated XAS spectra. (i) Left and right circular polarized light spectra recorded in normal incidence at 2 K and 6 T. The green curve represents the absolute XMCD integration. (j) XMCD spectrum ($C^+ - C^-$) for 30-nm film (blue) and bulk MnSi (green) together with the mathematical integration (red). p and q are the XMCD values at the corresponding energies, see text. (k) Magnetic field dependence of the XMCD loops at 2 and 50 K (above T_C) and bulk MnSi (VSM-SQUID) at 5, 25, and 30 K. (l) Temperature dependence of the Mn magnetic moment at 6 T for 15-nm and 30-nm MnSi films.

the atomic $2p$ and $3d$ spin-orbit couplings and local crystal-field parameters $10D_q$. To carry out the cluster calculations, we have assumed $10D_q = 1.8$ eV and the Slater integrals were calculated within the Hartree-Fock approximation [36]. Both the TEY and FY spectra of bulk MnSi are well simulated assuming mixed valence state with the corresponding spectral weights calculated by Carbone *et al.* [26] [21%d^7, 55%d^6, and 24%d^5, see Fig. 3(c) and Table I], showing that the XAS spectrum is dominated by Mn $3d^6$ configuration. Moreover, a good simulation of the 150-nm film spectrum is also obtained giving the same spectral weight to the d^6 electronic configuration in TEY and FY modes, but different electronic balance to d^7 and d^5. TEY of 150-nm film gives similar spectrum as the bulk, but a drastic enhancement of d^7 (33%) is needed to reproduce the high-energy peak of the L_2 edge, Fig. 3(d) and Table I. On the other side, 30-nm film shows an enhancement of the d^6 configuration (72% TEY and 60% FY) at expenses of decreasing the d^5. We point out that the simulations reported here show a qualitative analysis of the spectra based on the previous work by Carbone *et al.* [26] and this analysis shows a trend that should be baked with further photoemission and electronic structure calculations. In any case, since the strain induced by the substrate is negligible, as followed from the XRD lattice parameters, one might speculate with the nucleation of Mn^+ valence state at the MnSi/Si interface during the growth process and its stabilization throughout the entire film. We will return to this point in Sec. IV.

TABLE I. Weighted superposition of four single valence spectra for TEY and FY XAS.

	Electronic configuration (%)	d^7	d^6	d^5
Bulk	TEY	21	55	24
	FY [26]	24	55	21
150 nm	TEY	33	55	12
	FY	23	58	19
30 nm	TEY	20	72	8
	FY	22	60	18

Having established that the electronic structure is dominated by Mn^+ oxidation state in the thinnest MnSi films, next we carry out XMCD at the Mn $L_{2,3}$-edge to track the magnetism of the 30-nm-thick MnSi films, which turned out to be untraceable by VSM-SQUID. The integrated circular dichroism spectrum is defined as the absorption of the left circular polarized x rays (positive helicity, C^+) minus the absorption of right circular polarized x rays (negative helicity, C^-). The XMCD sum rules apply to a transition between two well-defined shells, for example, the transition from a $2p$ core state to $3d$ valence states in transition-metal systems and show that the integral over the XMCD signal of a given edge allows for the determination of the ground state expectation values of the orbital moment (L_z) and for the effective spin moment (S_z), since the integration of the $2p$-$3d$ x-ray absorption spectrum is proportional to the number of $3d$ states, ($\langle n_h \rangle$) [37].

The applied magnetic field was parallel to the incident beam and perpendicular to the sample surface plane and thereby, parallel to the [111] direction, as depicted in Fig. 3(a), which also mimics the magnetic field geometry of the Hall measurements presented in Sec. III E. The XMCD data were taken by tracking the energy dependence for left and right circular polarized light at the maximum field of 6 T. The integral

for the whole range, $L_3 + L_2$, can be precisely determined from the integrated spectrum, as illustrated in Fig. 3(i). The saturation behavior of the integration of the XMCD spectra near the end of the integrated spectra indicates that there is no significant XMCD signal at photon energies 30 eV above the L_2 white line. In order to measure the magnetic behavior of the thinnest films, we have performed magnetic field dependence of the maximum dichroic signal (Mn^+ edge, 640 eV). To transfer the dichroic signal to magnetization units, $m_{\rm orb}$ and $m_{\rm spin}$ can be calculated as $-4q(10 - n_{3d})/3r$ and $-(6p - 4q)(10 - n_{3d})/r$, where p, q, and r values are also obtained from the XMCD integration [37] and Figs. 3(i) and 3(j). We have used $n_{3d} = 6.1$ electrons as an average number obtained from the XAS calculation. At $T = 50$ K, Fig. 3(k), the field dependence magnetization loop follows a paramagnetic behavior as expected for temperatures above the magnetic transition. Temperature dependence of the magnetic moment of Mn at 6 T is plotted in Fig. 3(l) and follows qualitatively the behavior reported by SQUID magnetometry for thicker films. Remarkably, at the lowest temperature measured, $T = 2$ K, neither the magnetization saturates at the maximum applied ($H = 6$ T) nor hysteresis is observed. This result marks a difference of the magnetic behavior between thicker and thinner MnSi films. Fitting the $M(H)$ curve to the Langevin function gives a saturated magnetic moment of $\sim 0.7\,\mu_B$/Mn and $H_s^{\perp}$ at ~ 25 T, larger than the SQUID values obtained for the bulk and the 150-nm-thick film [Fig. 3(k)], thereby showing an enhancement of the Mn moment. This enhancement has been predicted by density-functional theory (DFT) at the MnSi/Si interface [38] and is also expected on the basis of the higher resistivity, as we will see next. Hence, our XMCD data indicates a spin disordered state at magnetic fields relevant to the analysis of the Hall data (see Sec. III E). This disordered state may arise from transition metal site disorder and nonstoichiometry, distorted helicoidal states or frustration between crystal domains with opposite chirality.

D. Field- and angular-dependent magnetoresistance

Next, we continue with the electric characterization of the thin MnSi films. The temperature dependence of the longitudinal resistivity, ρ_{xx}, of 150- and 30-nm-thick MnSi films [Fig. 4(a) and inset] shows a cusp related to the magnetic transition at 34 K [39], only observed in single crystals but not in samples grown by MBE or solid phase epitaxy (SPE) [17], evidencing the high quality of our films. The residual resistivity, ρ_{xx0}, extrapolated at $T \to 0$ K ~ 100 $\mu\Omega$ cm is independent of the MnSi thickness. The residual resistivity ratio, RRR $[\rho_{xx}(300\,\text{K})/\rho_{xx0}(5\,\text{K})] \sim 5$ (30-nm-thick MnSi), is comparable to thicker films of FeGe and does depend on the film thickness, showing a RRR ~ 3 for 150-nm-thick MnSi film due to the lower resistivity at 300 K. On the other hand, the ρ_{xx} for $T < T_C$ does not follow a T^2 dependence expected from the mutual scattering of fermion quasiparticles within the standard theory of metals [40,41]. In addition, ρ_{xx} for $T > T_C$ is not in agreement with the theoretical expectation of a linear dependence on the T due to phonon scattering.

In materials with magnetic ordering, spin-dependent transport originates from spin-orbit interaction, which causes the scattering rate of the conduction electrons, τ^{-1}, to depend

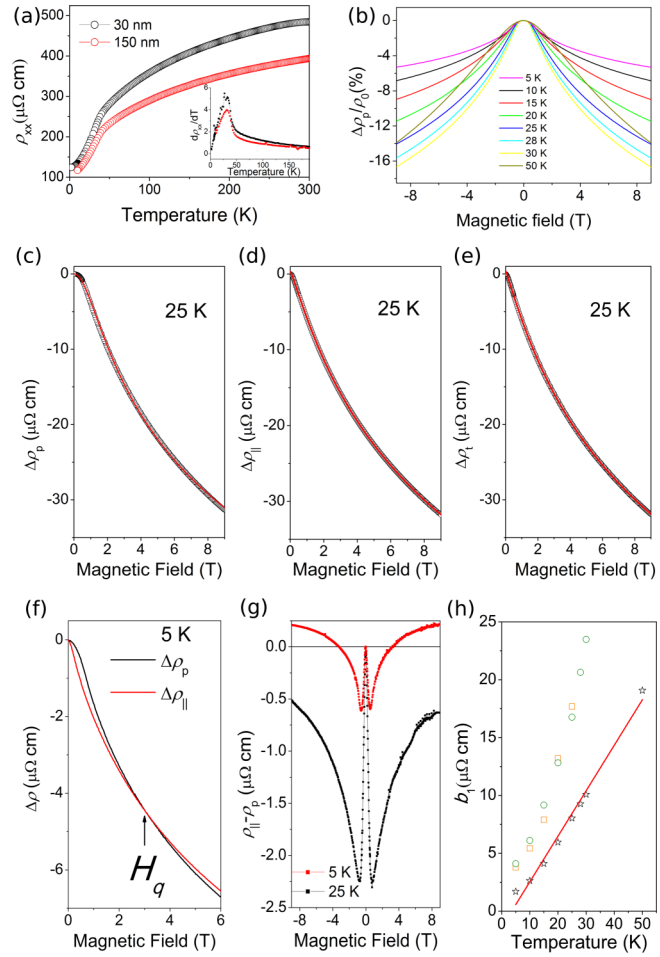

FIG. 4. [(a)–(f)] Longitudinal resistivity ρ_{xx} measured at zero field as a function of temperature for 30- and 150-nm-thick films. Inset, derivative of the resistivity vs temperature highlighting the magnetic transition T_C. (b) Perpendicular magnetoresistance, $(\rho_p - \rho_0)/\rho_0$, at various temperatures. [(c)–(e)] Representative fittings of $\Delta\rho_p$ ($\rho_p - \rho_0$, $\rho_{\parallel} - \rho_0$ and $\rho_t - \rho_0$). Red curves represent the fitting to the Khosla-Fisher equation for $\rho_p - \rho_0$ and Khosla-Fisher plus spin disorder for $\rho_{\parallel} - \rho_0$ and $\rho_t - \rho_0$. (f) Comparison of the longitudinal ($\Delta\rho_{\parallel}$) and perpendicular magnetoresistance ($\Delta\rho_p$) at 5 K. The arrow marks the transition from the spin-disorder to spin-fluctuation regime. (g) Difference between parallel and perpendicular resistivities ($\rho_{\parallel}$ and ρ_p) at 5 and 25 K. (h) Temperature dependence of the b_1 coefficient obtained at high field from the fitting to the Khosla-Fischer equation for ρ_p (open stars) and ρ_t and $\rho_{\parallel}$ (open circles and squares).

on the direction of magnetization M with respect to the current, the so-called *anisotropic magnetoresistance* (AMR) [40]. AMR is defined as $\Delta\rho/\rho \equiv (\rho_{\parallel} - \rho_t)/\rho_{\parallel}$. $\rho_{\parallel}$, ρ_t and ρ_p are the longitudinal resistivity measured with the magnetic field applied along the x (parallel to the current), y (transverse to the current) and z axis (perpendicular to the current, out-of-plane direction), respectively [see Figs. 5(a)–5(c) for a definition of the different geometries]. ρ_p is often considered similar to ρ_t within the AMR theory. To gain deeper insight into the scattering mechanisms of our films, we have performed field- and angular-dependent magnetoresistance (FDMR and ADMR). We focus on the 30-nm-thick MnSi film. The FDMR

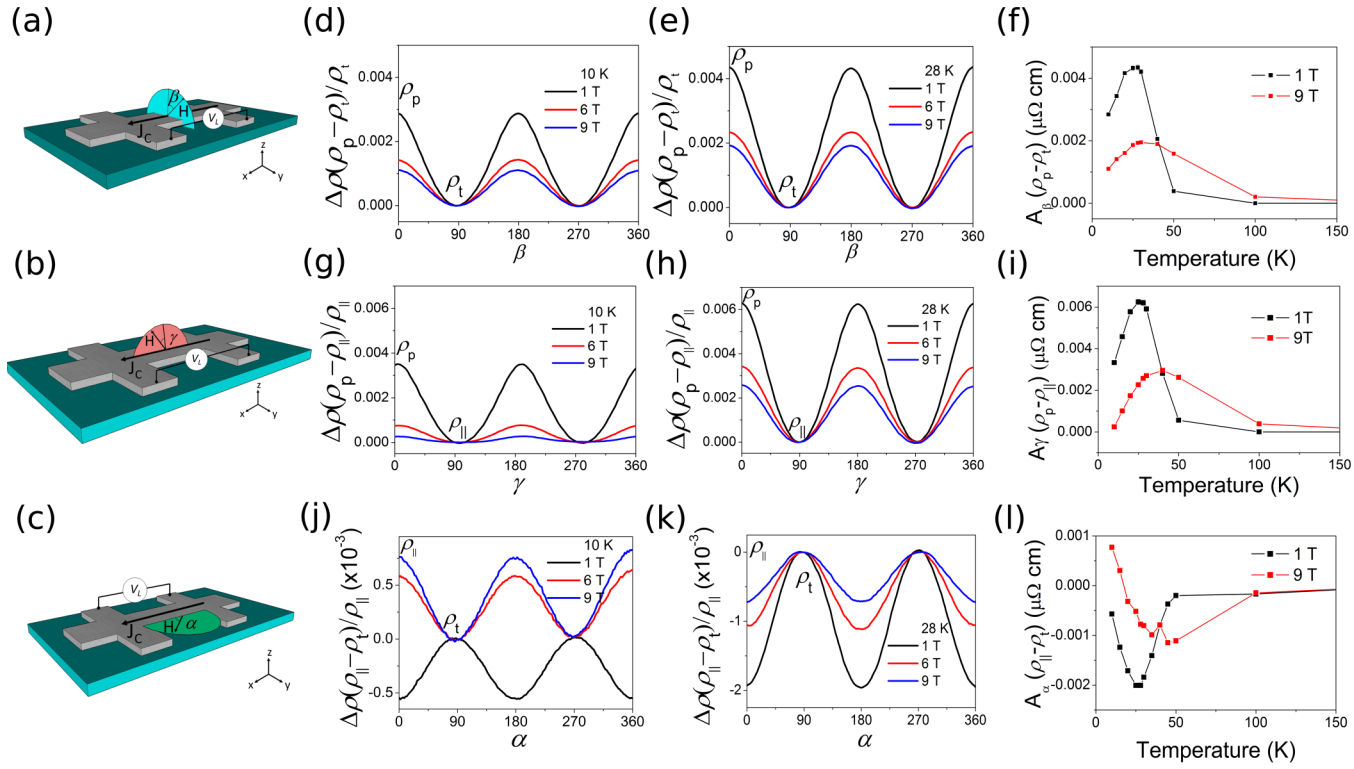

FIG. 5. [(a)–(c)] Geometries of the Hall bar used to measure the ADMR. J_c stands for the direction of the current and the angles of rotation are defined as the greek letters γ, β, and α. [(d) and (e)] ADMR for the β geometry at $T = 10$ and 28 K and (f) temperature dependence of the ADMR amplitude at 1 and 9 T. The same convention is used in (g)–(i) for γ and (j)–(l) for α geometries, see text.

is defined as $[\rho(H)\text{-}\rho_0]/\rho_0$, where $\rho(H)$ is either $\rho_\parallel$, ρ_p or ρ_t and ρ_0 is the resistivity at zero magnetic field.

The perpendicular FDMR, $\Delta\rho_p/\rho_0 \equiv (\rho_p - \rho_0)/\rho_0$ displays a negative contribution for magnetic fields parallel to z axis, (111) direction [Fig. 4(b)]. The observed negative FDMR reaches a value of 16% at 9 T and at temperatures close to the ordering temperature T_C, evidencing scattering from local moments and spin fluctuations that increase rapidly with temperature. Neither classical Lorentz-MR, which is positive and proportional to $(M + H)^2$, nor linear-MR due to elastic scattering of thermally excited magnons are observed. Linear MR has been reported for single crystals of MnSi and sputtered thin films of isostructural FeGe [21]. We need to point out that FeGe presents a magnetic moment of $\sim 3\,\mu_B$/Fe much higher than the $0.4\,\mu_B$/Mn characteristic of a weak itinerant ferromagnet and the $0.7\,\mu_B$/Mn obtained from the high-field extrapolation of the XMCD data. No hysteresis is observed in the FDMR curves, in agreement with the XMCD data thus, suggesting negligible contribution of magnetic domain structure.

The negative, nonlinear FDMR was fitted by the Khosla-Fischer model based on the *s-d* exchange Hamiltonian [42], which predicts the MR to follow:

$$\Delta\rho_p(H) = -b_1 \ln[1 + (b_2\mu_0 H)^n], \tag{4}$$

where b_1 and b_2 are complex parameters depending on the magnetization and temperature, respectively, and the critical exponent, $n = 2$, is characteristic of scattering of electrons by spin fluctuations [see Fig. 4(c) for a representative fitting]. In Fig. 4(h), a linear temperature dependence of the b_1 parameter for perpendicular FDMR is observed, reflecting the enhancement of the spin fluctuations with temperature. It is important to note that the Khosla-Fischer formula still holds at temperatures below the magnetic transition in good agreement with scattering by spin fluctuations and the absence of an ordered state observed by XMCD and the change in the magnetic/electronic structure reported by XAS. In fact, magnetotransport measurements also indicate that the Khosla-Fischer model is still valid for temperatures below T_N in thin FeGe films [21].

Remarkably, the parallel and transverse FDMR $\Delta\rho_\parallel$ and $\Delta\rho_t$ reflect a different behavior from the perpendicular FDMR, $\Delta\rho_p$. At 5 K and low magnetic fields, where the spin wave contribution vanishes and the AMR should prevail, a crossing of the FDMRs between $\Delta\rho_p$ and $\Delta\rho_\parallel$ is observed around 3 T [black arrow in Fig. 4(f)]. For the parallel and transverse FDMR, the Khosla-Fisher model still describes the field dependence resistivity for $H > 3$ T, but, nevertheless, gives an odd fitting at low fields. In Fig. 4(g), we plot $\rho_\parallel - \rho_p$ which shows that the predictions of the AMR theory are fulfilled at high magnetic fields and low temperature (red curve). This situation is reversed at high temperature (black curve), as a consequence of the enhancement of spin fluctuations on approaching T_C developing its maximum amplitude at 1 T, as shown by a dip. The parallel and transverse FDMRs are better described by a assuming a combination of spin-disorder ($H <$ 3 T) and spin fluctuations ($H > 3$ T) dependence MR, where the spin-disorder term is based on the Edwards-Anderson

(EA) type model and given by [43]

$$\Delta\rho_{(\parallel,t)}(H) \approx -c(T,H) \times H^m. \quad (5)$$

We find that the critical exponent m is temperature dependent, ranging between ∼1.5 at 5 K and ∼1 at higher temperatures. Transverse FDMR measured in diluted alloys containing transition metal impurities also reported $m > 1$ below the freezing temperature T_0 [43], and temperature dependence of c. In any case, we identify the crossing field H_q as the field where the EA model for spin-glasses holds. Nevertheless, a critical value of $m = 2$, characteristic of a canonical spin-glass is found to give an odd fitting of the low-field FDMR, as expected since the effects of the spin dynamics are largely ignored within the EA model. Above the crossover field H_q, the FDMR is fitted following Eq. (3) giving values for the b_1 coefficient plotted in Fig. 4(h).

Figure 5 shows the angular dependence magnetoresitance (ADMR) curves as a function of magnetic field for representative temperatures following the geometries drawn in Figs. 5(a)–5(c). In the β geometry, the sample is rotated such that the external current is always perpendicular to the magnetic field while in the α and γ geometries, the rotation contains perpendicular/transverse contributions of the magnetic field to the AMR. The spin dependent scattering and spin-orbit interaction in a ferromagnet indicates that the AMR follows $\Delta\rho = \rho_\parallel - \rho_\perp > 0$, where $\rho_\perp$ is either ρ_p or ρ_t. We want to point out that, despite the 30-nm-thick MnSi film is not saturated at 9 T, the AMR rules should still hold below the saturation field. These dictations state that the spin-dependent scattering should be constant under rotation in the β geometry. As depicted in Figs. 5(d) and 5(e), the ADMR follows a $\cos^2(\beta)$ with $\rho_p > \rho_t$, therefore, violating the derivations of the AMR theory for ferromagnets. Deviations of the AMR theory have been reported in textured Fe, Co and NiFe films and attributed to geometrical size effects (GSE) [44]. Although the nature of the GSE is still under discussion, its origin might include the change of the electronic structure [45], anisotropic interfacial scattering [46] and textured-induced anisotropic *sd* scattering [47]. Putting together our XAS measurements and the violations of the AMR theory, the enhancement of the d^6 orbital occupation and the anisotropic mixing of the $3d$ levels near the Fermi level play an essential role in the magnetotransport properties of MnSi thin films. Temperature dependence of ADMR [Fig. 5(f)] shows an enhancement of its amplitude up to T_C due to the enhancement of the scattering of electrons with spin fluctuations on approaching the magnetic transition, in good agreement with the FDMR of Fig. 4(b). The amplitude of the ADMR is lower at 9 T due to the damping of magnetic fluctuations with magnetic field. In addition, ADMR(γ) ∼ ADMR(β), where ADMR(γ) follows a $\cos^2(\gamma)$, also contradicts the AMR theory [Figs. 5(g) and 5(h)].

The situation changes drastically when measuring ADMR in α geometry [Figs. 5(j) and 5(k)]. At low temperatures, below $T \leqslant 15$ K, we observe a change in the sign of the amplitude of the AMR as a function of the magnetic field, Fig. 5(j). At higher temperatures, the ADMR follows a $\cos^2(\alpha)$ for all the magnetic fields, presumably due to a change of the spin-dependent scattering of the majority and minority channels. Despite the change of sign with magnetic field, the amplitude of the signal follows the same temperature behavior as for γ and β geometries [Figs. 5(i) and 5(l)] indicating temperature dependent spin fluctuations mediated magnetoresistance. More detailed work on the GSE, considering also interfacial and surface scattering, is needed to resolve each contribution.

E. Hall effect and topological resistivity

We have performed Hall measurements to search for indications of topological order in our thin MnSi films, which has been considered as a strong hallmark for the existence of skyrmions. The total Hall resistivity ρ_H is defined as a combination of three contributions:

$$\rho_H = \rho_{xy} = \rho_{xy}^O + \rho_{xy}^A + \rho_{xy}^{\mathrm{TH}}, \quad (6)$$

where ρ_{xy}^O and ρ_{xy}^A are the ordinary and anomalous Hall resistivities and ρ_{xy}^{TH} is the topological Hall contribution due to the existence of nontrivial spin textures. ρ_{xy}^O is driven by the Lorentz force exerted by the electrons under the influence of a magnetic field H perpendicular to the film plane ($\rho_{xy}^O = R_0 H_\perp$, where R_0 is the ordinary Hall coefficient) and ρ_{xy}^A is proportional to the anomalous Hall coefficient, R_S, and the out-of-plane magnetization, $M_\perp$. It turns out that, in Eq. (6), the value $M_\perp$ must contain the magnetization of the MnSi film (without the substrate), as this is the only contribution to the Hall resistivity.

Although the ordinary Hall effect is well understood and follows a linear behavior with the magnetic field, the anomalous contribution is still under a big debate [22]. Considering only the *intrinsic* contribution, the anomalous Hall effect, ρ_{xy}^A, can be described as

$$\rho_{xy}^A = R_S M_\perp = S_A M_\perp \rho_{xx}^2, \quad (7)$$

where S_A is a coefficient directly related to the intrinsic anomalous Hall conductivity.

The ρ_{xy}^{TH} due to the presence of nontrivial spin textures, such as skyrmions, follows:

$$\rho_{xy}^{\mathrm{TH}} = n_{Skx} P R_{\mathrm{TH}} B_{\mathrm{eff}}, \quad (8)$$

where n_{Skx} is the relative skyrmion density, P is the polarization of the conduction electrons, R_{TH} is the topological Hall coefficient, and B_{eff} is the effective magnetic field derived from the real-space Berry phase.

As the topological Hall resistivity should vanish in the spin collinear state at $H > H_C$, we can determine R_0 and S_A from the linear fitting of $\rho_{xy}^{\mathrm{exp}}/H$ vs $\rho_{xx}^2 M_\perp/H$ between 3 and 6 T, [14,27,30]. For thick MnSi films (150 nm), we report a value of $R_0 = -3.74 \times 10^{-8}$ Ω cm/T, a nearly temperature independent $S_A = 11.1 \times 10^{-6}$ $(\mu\Omega\ \mathrm{cm}\ \mu_B)^{-1}$ and carrier densities $n_e \sim 2(1) \times 10^{22}\,\mathrm{cm}^{-3}$ at 25 K. The value S_A is positive for FeGe thin films [27,30] and for $Fe_{1-x}Co_xSi$ [8], whereas it is negative for bulk MnSi. Sign changes in S_A can be related to changes in the majority and minority spin channels and also to changes in sign of the spin-orbit coupling (SOC).

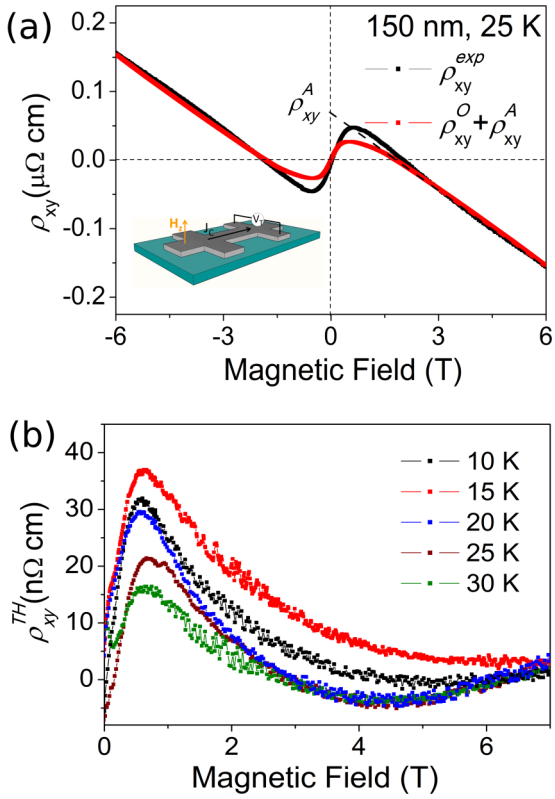

FIG. 6. (a) Experimentally measured Hall resistivity, $\rho_{xy}^{\rm exp}$ at 25 K for a 150-nm-thick film (black curve) and the modeled ordinary ρ_{xy}^{O} and anomalous ρ_{xy}^{A}, Hall contributions (red curve). (Inset) geometry used to measure the Hall resistivity. (b) Topological Hall resistivity $\rho_{xy}^{\rm TH}$ obtained after subtraction of the ρ_{xy}^{O} and ρ_{xy}^{A} to the $\rho_{xy}^{\rm exp}$ for different temperatures. See text for details.

The calculated ordinary and anomalous Hall resistivity is plotted as a red curve in Fig. 6(a) using the $M_{\perp}$ values obtained from the SQUID measurements. The difference between the experimental and calculated Hall resistivity, termed in the literature as *topological* Hall resistivity, is shown in Fig. 6(b) at various temperatures. $\rho_{xy}^{\rm TH}$ is present at all temperatures below T_C, in contrast to bulk MnSi, where $\rho_{xy}^{\rm TH}$ presents only a nonzero value in a very narrow temperature range close to the ordering temperature, $T_C = 30$ K. $\rho_{xy}^{\rm TH}$ presents a sharp upturn at low fields but smoothly vanishes at large H, due to the uncertainty in subtracting the small topological contribution to the Hall data. At high fields, $\rho_{xy}^{\rm TH}$ disappears since the induced ferromagnetism has no spin chirality.

The presence of this topological Hall resistivity is usually assumed as an indication of the presence of magnetic skyrmions. The absolute value of the $\rho_{xy}^{\rm TH}$ is temperature dependent and has a maximum value of $+37$ nΩ cm, larger than thin films grown by MBE ($+10$ nΩ cm) [14,17] and the bulk ($+4$ nΩ cm) [9] but with a similar value of the helical wavelength $\lambda_D \sim 18$ nm. $\rho_{xy}^{\rm TH}$ is lower than that reported for policrystalline MnGe (-160 nΩ cm) [28] and thin films of FeGe (-150 nΩ cm) [30], which hosts more localized moments and higher transition temperature, $T_C = 271$ K. The topological Hall resistivity shows a maximum at 15 K and 0.7 T, therefore reflecting a temperature dependence of the real-space fictitious magnetic field experienced by the electrons as they adiabatically follow the magnetization of the chiral magnet. Temperature dependence of $\rho_{xy}^{\rm TH}$ has been also reported for sputtered films of FeGe [27,30] and MnGe [28].

Shown in Figs. 7(a)–7(g) is the experimental Hall resistivity at low temperature for the 30-nm-thick film. However, unlike thicker films, we clearly distinguish three regimes: (i) a temperature dependent hysteresis at low fields, zoomed-in in Fig. 7(h) (ii) a magnetic reversal behavior at intermediate fields and (iii) a linear behavior at high fields. Features (ii) and (iii) are observed in the 150-nm-thick films analyzed before and ascribed them to anomalous and ordinary Hall effect. As the temperature increases, the hysteresis continues to increase up to T_C, reaching a maximum value of 0.3 T at 25 K, see Fig. 7(h). We point out that the XMCD data does not show hysteresis in the magnetic properties of the 30-nm-thick MnSi film, therefore we cannot associate the hysteresis in the Hall data to the low temperature magnetization. Moreover, on approaching the magnetic transition, there is a nonlinearity in the Hall effect, Figs. 7(f) and 7(g), perhaps arising from different carrier types, with different ordinary Hall coefficients [21]. Following the previous analysis, we fit first the Hall data assuming the magnetization of bulk MnSi and thick films ($0.4\,\mu_B$). This procedure gives an estimation of the ordinary and anomalous Hall resistivity plotted as a green curve in Fig. 7(i). As observed, by using the 150-nm-thick MnSi film magnetic data, the experimental and calculated Hall resistivity matches at high fields, thus giving a *topological* Hall resistivity plotted in Fig. 7(j) at different temperatures. In addition, the topological signal develops a peak at 1 T at low temperature and at fields close to those of the thicker films. This maximum signal gets suppressed with temperature and evolves towards a dip at lower fields on approaching T_C. Remarkably, the sign of $\rho_{xy}^{\rm TH}$ is opposite but the same size to that of 150-nm-thick film, -30 nΩ cm at 30 K. This behavior has been reported for MBE MnSi [14] and sputtered FeGe thin films [27] and attributed to a change in the spin polarization (P) of the charge carriers with temperature.

However, the analysis of the Hall resistivity relies on a comprehensive knowledge of the magnetization $M_{\perp}$ and it turns out that the out-of-plane magnetic properties for thin films of MnSi ($\leqslant 30$ nm) do not follow either the bulk behavior or the thick films behavior, as we have extensively analyzed by XMCD. Using the XMCD data to fit the Hall effect reveals non zero $\rho_{xy}^{\rm TH}$ at high fields changing sign below 4 T, [red curve in Fig. 7(k)]. Besides, the *topological* signal at low fields is always positive with a maximum value $\rho_{xy}^{\rm TH} \sim 45$ nΩ cm at 25 K. The magnetization of the 30-nm-thick film obtained from the XMCD data indicates that the analysis of the Hall data is not straightforward since between 3 and 6 T the Hall signal still corresponds to a combination of ordinary and anomalous contributions and cannot be easily singled out following the analysis reported in literature. It is likely that the $\rho_{xy}^{\rm TH}$ in Fig. 7(j) is a byproduct of the analysis procedure due to the difficulty in the estimation of the $\rho_{xy}^{\rm TH}$ buried in a large $\rho_{xy}^{\rm exp}$.

IV. DISCUSSION

We have optimized the growth of high-quality textured (111) thin MnSi films without indications of impurity phases

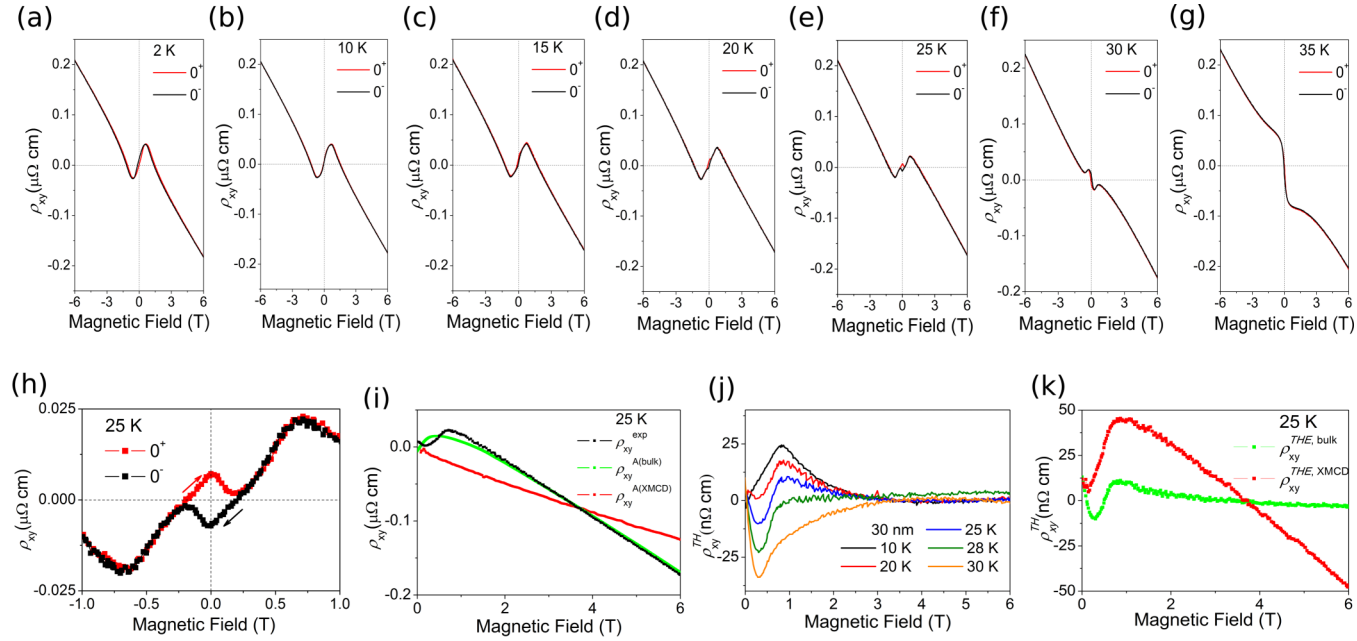

FIG. 7. [(a)–(g)] Hall resistivity for a 30-nm MnSi thin film for selected temperatures. (h) Zoom-in of the low-field Hall data at 25 K, showing the low-field hysteresis. 0^+ and 0^- denote the direction of the ramping field (0^+ : -9 T $\rightarrow$ 9 T and 0^- : 9 T $\rightarrow$ -9 T) (i) Modeling of the ρ_{xy}^O and ρ_{xy}^A assuming the bulk magnetization (green curve) and the measured by XMCD (red curve). (j) ρ_{xy}^{TH} obtained from the subtraction of the calculated Hall using the magnetization of the thick film to the experimentally data. (k) ρ_{xy}^{TH} after subtraction of the AHE obtained by using the XMCD data at 25 K and its comparison with ρ_{xy}^{TH} obtained by using the thick film magnetization data.

as observed by XRD, electron diffraction and HRTEM. Moreover, lattice parameters obtained from XRD match the bulk value independently of the film thickness, allowing us to study the magnetic and electronic properties of MnSi films without being affected by substrate-induced strain. Our thick MnSi films ($d = 150$ nm) develop magnetic and electronic properties which resemble to the bulk counterpart and topological Hall signal similar to that reported in the literature and previous reports [13,14]. A careful analysis of the magnetization shows an enhancement of the magnetic anisotropy which has been theoretically predicted to stabilize nontrivial spin textures. Nevertheless, the value of K/K_0 we have shown cannot be explained by strain related micromagnetic models, as our MnSi films are strain-free. This experimental result points to a change in the electronic structure that plays a leading role in the enhancement of the magnetic anisotropy K, as evidenced by XAS. It is likely that the modification of orbital occupation happens initially at the MnSi/Si interface, as a consequence of the epitaxial growth at high temperatures and further relaxation with the thickness. Stabilization of new electronic, magnetic and charge structures via epitaxial growth have been demonstrated in metals and transition metal oxides (see, for instance, Refs. [48,49]). This also indicates that the absence of long-range magnetic ordering for thinner MnSi films ($d <$ 30 nm) is, presumably, related to the stabilization on Mn^+ oxidation state and domains of opposite chiralities, although interface induced defects during growth may also enhance the magnetic frustration/disorder. The electronic structure and magnetization data obtain by XAS and XMCD leads to explain the anisotropic magnetoresistance and the violation of the angular dependence magnetoresistance dictations in terms of geometrical size effects. Although we point to changes in the electronic structure as the main source for the GSE, a more careful study is required to understand the three mechanisms outlined in the text.

Our comprehensive set of data have important implications for the analysis and interpretation of the Hall effect. The major drawback in extracting the anomalous contribution to the Hall resistance is the precise knowledge of the momentum dependence Berry phase that acquire the electrons in a ferromagnet. This quantity is related to the magnetization and SOC of material and, as we have seen, it turns out to be difficult to obtain for thin MnSi. While both M_S and ρ_{xy}^{TH} are in agreement with literature for 150-nm-thick film, 30-nm-thick MnSi does not develop long-range magnetic order and remain spin disordered at the magnetic fields relevant for the analysis of the Hall effect. Remarkably, the Hall effect for 30-nm thick MnSi presents a hysteresis behavior at low fields and formerly interpreted as extended zero field high density of skyrmions. The magnetization obtained from the XCMD experiments fails to fit the Hall data at high fields hence, the mechanism behind the anomalous and topological Hall coefficient should adopt a rather complex function of the resistivity.

In general, ρ_{xy}^A is proportional to the *intrinsic* contribution related with the band structure and spin-orbit coupling, the so-called momentum-space Berry-phase. In Fig. 8, we plot the anomalous Hall resistivity ρ_{xy}^A vs ρ_{xx}^2 at 6 T that does not reveal a linear dependence below T_C, suggesting that the anomalous Hall effect also has contributions from other mechanisms. Besides the *intrinsic* contribution to the anomalous Hall response, *extrinsic skew scattering* and *side jump contributions* caused by impurities and defects are

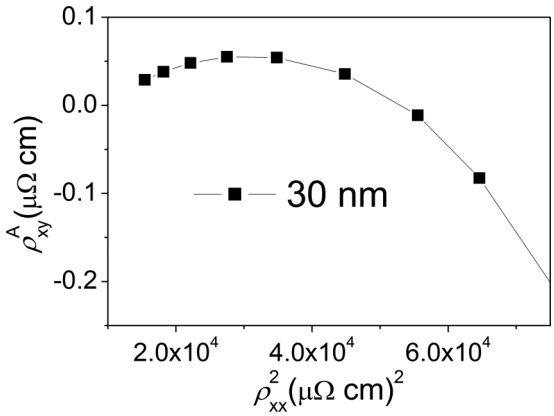

FIG. 8. Anomalous Hall resistivity vs squared longitudinal resistivity below T_C in 30-nm-thick MnSi film.

usually relevant. However, since *skew scattering* and *side jump* mechanisms are proportional to ρ_{xx0} and ρ^2_{xx0}, they cannot explain the behavior in Fig. 8. This suggests that the intrinsic contribution to the anomalous Hall effect, S_A, is not constant due to the change of magnetic texture with the temperature and magnetic field. This is supported by the high values of magnetoresistance ($\sim$16%) we have measured. Furthermore, cross-term contributions with multiple competing scattering mechanisms should not be neglected [50].

Despite further work is needed to elucidate the microscopic mechanisms stabilizing the zero-field *topological* Hall effect, it seems plausible that any possible skyrmion phase in our thin films may arise from topological excitations in the disordered state of MnSi. It has been shown that the Hall resistivity in the solid solution $Mn_{1-x}Fe_xSi$ reveals the emergence of a topological signal in the *fluctuation disordered* (FD) regime at $T > T_C$, thereby electrons can acquire an anomalous velocity above the transition temperature [8]. This demonstrates the extreme sensitivity of the THE to details of the electronic structure and breakdown of the adiabatic approximation due to possible mixtures of real- and momentum-space Berry phases. Further, in the FD regime, the THE may extend to a larger fields as compared with the skyrmion lattice phase and can even emerge at $H = 0$. Therefore it is reasonable to assume that our thin films of MnSi behave similarly as the FD regime of $Mn_{1-x}Fe_xSi$ as the helical phase is suppressed.

V. CONCLUSIONS

The electronic structure, field and angular dependence magnetoresitance and Hall effect have been measured in textured (111) MnSi. We have observed an extended zero field *topological* order in 30-nm-thick MnSi films similar to that reported for FeGe [27,30]. Our main result is that the change of the electronic structure and the stabilization of the Mn^+ oxidation state for thinner MnSi films should be taken into account along with the modification of the anisotropy ratios, K/K_c for the stabilization of the nontrivial topological spin textures. We have also reported by XMCD a spin disordered ground state for thin MnSi films, leading to a modification of the momentum space Berry phase and SOC connected to the anomalous Hall resistivity. The implications of our XAS and XMCD results point to changes in the *intrinsic* contribution of the anomalous Hall conductivity, although contributions due to scattering by impurities and disorder might also play a crucial role in the stabilization of the *topological* order in a broader range of magnetic fields. Further experimental work is required to resolve the microscopic mechanisms behind geometric size effects and the Hall resistivity in MnSi thin films.

ACKNOWLEDGMENTS

Y. Lu and E. Sagasta are acknowledged for fruitful discussions and critical reading of the manuscript. We acknowledge the Spanish MINECO under the Maria de Maeztu Units of Excellence Programme - MDM-2016-0618 and under the Project No. 2015-65159-R. S.B.-C. thanks IKERBASQUE for financial support. J.M.G.-P. thanks the Spanish MINECO for a Ph.D. fellowship (Grant No. BES-2016-077301). The research in Dresden is supported by the Deutsche Forschungsgemeinschaft through Grant No. 320571839.

[1] S. Mühlbauer, B. Binz, F. Jonietz, C. Pfleiderer, A. Rosch, A. Neubauer, R. Georgii, and P. Böni, Science **323**, 915 (2009).
[2] F. Jonietz, S. Muhlbauer, C. Pfleiderer, A. Neubauer, W. Münzer, A. Bauer, T. Adams, R. Georgii, P. Boni, R. A. Duine, K. Everschor, M. Garst, and A. Rosch, Science **330**, 1648 (2010).
[3] A. Fert, N. Reyren, and V. Cros, Nat. Rev. Mater. **2**, 17031 (2017).
[4] H. Wilhelm, M. Baenitz, M. Schmidt, U. K. Rößler, A. A. Leonov, and A. N. Bogdanov, Phys. Rev. Lett. **107**, 127203 (2011).
[5] E. Moskvin, S. Grigoriev, V. Dyadkin, H. Eckerlebe, M. Baenitz, M. Schmidt, and H. Wilhelm, Phys. Rev. Lett. **110**, 077207 (2013).
[6] Y. Onose, Y. Okamura, S. Seki, S. Ishiwata, and Y. Tokura, Phys. Rev. Lett. **109**, 037603 (2012).
[7] W. Münzer, A. Neubauer, T. Adams, S. Mühlbauer, C. Franz, F. Jonietz, R. Georgii, P. Böni, B. Pedersen, M. Schmidt, A. Rosch, and C. Pfleiderer, Phys. Rev. B **81**, 041203(R) (2010).
[8] C. Franz, F. Freimuth, A. Bauer, R. Ritz, C. Schnarr, C. Duvinage, T. Adams, S. Blügel, A. Rosch, Y. Mokrousov, and C. Pfleiderer, Phys. Rev. Lett. **112**, 186601 (2014).
[9] T. Schulz, R. Ritz, A. Bauer, M. Halder, M. Wagner, C. Franz, C. Pfleiderer, K. Everschor, M. Garst, and A. Rosch, Nat. Phys. **8**, 301 (2012).
[10] A. Bauer, A. Neubauer, C. Franz, W. Münzer, M. Garst, and C. Pfleiderer, Phys. Rev. B **82**, 064404 (2010).
[11] C. Thessieu, C. Pfleiderer, A. N. Stepanov, and J. Flouquet, J. Phys.: Condens. Matter **9**, 6677 (1997).
[12] A. Bauer and C. Pfleiderer, Phys. Rev. B **85**, 214418 (2012).

[13] A. Neubauer, C. Pfleiderer, B. Binz, A. Rosch, R. Ritz, P. G. Niklowitz, and P. Böni, Phys. Rev. Lett. **102**, 186602 (2009).
[14] Y. Li, N. Kanazawa, X. Z. Yu, A. Tsukazaki, M. Kawasaki, M. Ichikawa, X. F. Jin, F. Kagawa, and Y. Tokura, Phys. Rev. Lett. **110**, 117202 (2013).
[15] X. Yu, J. P. DeGrave, Y. Hara, T. Hara, S. Jin, and Y. Tokura, Nano Lett. **13**, 3755 (2013).
[16] A. B. Butenko, A. A. Leonov, U. K. Rößler, and A. N. Bogdanov, Phys. Rev. B **82**, 052403 (2010).
[17] S. A. Meynell, M. N. Wilson, H. Fritzsche, A. N. Bogdanov, and T. L. Monchesky, Phys. Rev. B **90**, 014406 (2014).
[18] F. N. Rybakov, A. B. Borisov, S. Blügel, and N. S. Kiselev, Phys. Rev. Lett. **115**, 117201 (2015).
[19] E. Karhu, S. Kahwaji, T. L. Monchesky, C. Parsons, M. D. Robertson, and C. Maunders, Phys. Rev. B **82**, 184417 (2010).
[20] M. N. Wilson, E. A. Karhu, A. S. Quigley, U. K. Rößler, A. B. Butenko, A. N. Bogdanov, M. D. Robertson, and T. L. Monchesky, Phys. Rev. B **86**, 144420 (2012).
[21] N. A. Porter, J. C. Gartside, and C. H. Marrows, Phys. Rev. B **90**, 024403 (2014).
[22] N. Nagaosa, J. Sinova, S. Onoda, A. H. MacDonald, and N. P. Ong, Rev. Mod. Phys. **82**, 1539 (2010).
[23] S. A. Meynell, M. N. Wilson, J. C. Loudon, A. Spitzig, F. N. Rybakov, M. B. Johnson, and T. L. Monchesky, Phys. Rev. B **90**, 224419 (2014).
[24] E. A. Karhu, S. Kahwaji, M. D. Robertson, H. Fritzsche, B. J. Kirby, C. F. Majkrzak, and T. L. Monchesky, Phys. Rev. B **84**, 060404(R) (2011).
[25] M. N. Wilson, E. A. Karhu, D. P. Lake, A. S. Quigley, S. Meynell, A. N. Bogdanov, H. Fritzsche, U. K. Rößler, and T. L. Monchesky, Phys. Rev. B **88**, 214420 (2013).
[26] F. Carbone, M. Zangrando, A. Brinkman, A. Nicolaou, F. Bondino, E. Magnano, A. A. Nugroho, F. Parmigiani, Th. Jarlborg, and D. van der Marel, Phys. Rev. B **73**, 085114 (2006).
[27] J. C. Gallagher, K. Y. Meng, J. T. Brangham, H. L. Wang, B. D. Esser, D. W. McComb, and F. Y. Yang, Phys. Rev. Lett. **118**, 027201 (2017).
[28] N. Kanazawa, Y. Onose, T. Arima, D. Okuyama, K. Ohoyama, S. Wakimoto, K. Kakurai, S. Ishiwata, and Y. Tokura, Phys. Rev. Lett. **106**, 156603 (2011).
[29] E. A. Karhu, U. K. Rößler, A. N. Bogdanov, S. Kahwaji, B. J. Kirby, H. Fritzsche, M. D. Robertson, C. F. Majkrzak, and T. L. Monchesky, Phys. Rev. B **85**, 094429 (2012).
[30] S. X. Huang and C. L. Chien, Phys. Rev. Lett. **108**, 267201 (2012).
[31] M. L. Plumer and M. B. Walker, J. Phys. C **14**, 4689 (1981).
[32] S. V. Maleyev, Phys. Rev. B **73**, 174402 (2006).
[33] J. Stöhr and H. C. Siegmann, *Magnetism From Fundamentals to Nanoscale Dynamics*, Springer Series in Solid-State Sciences (Springer-Verlag, Berlin, Heidelberg, 2006).
[34] M. W. Haverkort, M. Zwierzycki, and O. K. Andersen, Phys. Rev. B **85**, 165113 (2012).
[35] Y. Lu, M. Höppner, O. Gunnarsson, and M. W. Haverkort, Phys. Rev. B **90**, 085102 (2014).
[36] M. Haverkort, Spin and orbital degrees of freedom in transition metal oxides and oxide thin films studied by soft x-ray spectroscopy, Ph.D. thesis, Universität zu Köln, 2005.
[37] C. T. Chen, Y. U. Idzerda, H.-J. Lin, N. V. Smith, G. Meigs, E. Chaban, G. H. Ho, E. Pellegrin, and F. Sette, Phys. Rev. Lett. **75**, 152 (1995).
[38] M. Hortamani, P. Kratzer, and M. Scheffler, Phys. Rev. B **76**, 235426 (2007).
[39] K. Kadowaki, K. Okuda, and M. Date, J. Phys. Soc. Jpn. **51**, 2433 (1982).
[40] B. Pippard, *Magnetoresistance in Metals* (Cambridge University Press, Cambridge, 1989).
[41] M. Otero-Leal, F. Rivadulla, S. S. Saxena, K. Ahilan, and J. Rivas, Pys. Rev. B **79**, 060401 (2009).
[42] R. P. Khosla and J. R. Fischer, Phys. Rev. B **2**, 4084 (1970).
[43] A. K. Nigam and A. K. Majumdar, Phys. Rev. B **27**, 495 (1983).
[44] L. K. Zou, Y. Zhang, L. Gu, J. W. Cai, and L. Sun, Phys. Rev. B. **93**, 075309 (2016).
[45] T. T. Chen and V. A. Marsocci, J. Appl. Phys. **43**, 1554 (1972).
[46] T. G. S. M. Rijks, S. K. J. Lenczowski, R. Coehoorn, and W. J. M. de Jonge, Phys. Rev. B **56**, 362 (1997).
[47] W. Gil, D. Görlitz, M. Horisberger, and J. Kötzler, Phys. Rev. B **72**, 134401 (2005).
[48] M. Bluschke, A. Frano, E. Schierle, D. Putzky, F. Ghorbani, R. Ortiz, H. Suzuki, G. Christiani, G. Logvenov, E. Weschke, R. J. Birgeneau, E. H. da Silva Neto, M. Minola, S. Blanco-Canosa, and B. Keimer, Nat. Commun. **9**, 2978 (2018).
[49] J. Engelmann, V. Grinenko, P. Chekhonin, W. Skrotzki, D. V. Efremov, S. Oswald, K. Iida, R. Hühne, J. Hänisch, M. Hoffmann, F. Kurth, L. Schultz, and B. Holzapfel, Nat. Commun. **4**, 2877 (2013).
[50] D. Hou, G. Su, Y. Tian, X. Jin, S. A. Yang, and Q. Niu, Phys. Rev. Lett. **114**, 217203 (2015).